Journal of Power Sources 196 (2011) 9459–9466

Contents lists available at ScienceDirect

Journal of Power Sources

journal homepage: www.elsevier.com/locate/jpowsour

High performance metal-supported solid oxide fuel cells with Gd-doped ceria barrier layers

Trine Klemensø[a,*], Jimmi Nielsen[a], Peter Blennow[a], Åsa H. Persson[a], Tobias Stegk[a], Bjarke Holl Christensen[b], Steffen Sønderby[b,c]

[a] Fuel Cells and Solid State Chemistry Division, Risø National Laboratory for Sustainable Energy, Technical University of Denmark, Frederiksborgvej 399, 4000 Roskilde, Denmark
[b] The Tribology Centre, Danish Technological Institute, Teknologiparken, Kongsvang Allé 29, 8000 Århus C, Denmark
[c] Thin Film Physics Division, Department of Physics, Chemistry and Biology, Linköping University, SE-581 83 Linköping, Sweden

ARTICLE INFO

Article history:
Received 15 March 2011
Received in revised form 24 May 2011
Accepted 5 July 2011
Available online 12 July 2011

Keywords:
SOFC
Metal-supported
Barrier layer
Magnetron sputtering
Durability

ABSTRACT

Metal-supported solid oxide fuel cells are believed to have commercial advantages compared to conventional anode (Ni–YSZ) supported cells, with the metal-supported cells having lower material costs, increased tolerance to mechanical and thermal stresses, and lower operational temperatures. The implementation of a metallic support has been challenged by the need to revise the cell fabrication route, as well as electrode microstructures and material choices, to compete with the energy output and stability of full ceramic cells.

The metal-supported SOFC design developed at Risø DTU has been improved, and an electrochemical performance beyond the state-of-the-art anode-supported SOFC is demonstrated possible, by introducing a CGO barrier layer in combination with Sr-doped lanthanum cobalt oxide (LSC) cathode. Area specific resistances (ASR) down to 0.27 $\Omega\,cm^2$, corresponding to a maximum power density of 1.14 $W\,cm^{-2}$ at 650 °C and 0.6 V, were obtained on cells with barrier layers fabricated by magnetron sputtering. The performance is dependent on the density of the barrier layer, indicating Sr^{2+} diffusion is occurring at the intermediate SOFC temperatures. The optimized design further demonstrate improved durability with steady degradation rates of 0.9% kh^{-1} in cell voltage for up to 3000 h galvanostatic testing at 650 °C and 0.25 A cm^{-2}.

1. Introduction

Solid oxide fuel cells are high-temperature electrochemical devices converting the chemically bound energy of e.g. hydrogen, methanol, ammonia, natural gas or biogas, directly into electric energy and heat. Inherently, the technology offers high efficiencies and fuel flexibility, and is therefore an attractive energy conversion technology.

The primary challenges for the commercialization of the technology are considered to be costs and durability. To accommodate this, research is pushing towards lower cell operation temperature (intermediate temperature SOFC, IT-SOFC) in the range of 500–700 °C. The lower temperatures involve advantages such as wider and cheaper choice of materials (e.g. metals), increased material durability, and increased system stability [1–3].

Metal-supported SOFCs are attractive cell designs for intermediate temperature operation. In addition to lower material cost of the metal, the metal-supported cells promise higher robustness due to higher thermal conductivity compared to ceramic supported SOFC, and the ductility of a metallic substrate. The improved robustness is advantageous in both the fabrication line as well as during operation. For some applications, such as APU (auxiliary power unit) and other small-scale systems, tolerance to dynamic operation, including fast start-up, thermal cycling, electric load transients, redox cycling, and shock vibrations, is essential [3,4].

The metal-supported SOFC development has been widely challenged by the cell fabrication. The classical and cheap wet ceramic processing combined with co-sintering requires the sintering to be carried out in reducing atmosphere, to avoid corrosion of the steel component at the high sintering temperatures needed for densification of the electrolyte. Alternatively, more complex methods can be used to deposit the electrolyte layer on a preformed or presintered metal substrate, these including pulsed laser deposition, electrophoretic deposition, plasma- and flame-spray [3–5].

Furthermore, the conventional and good-performing Ni–YSZ (yttria-stabilized zirconia) anode is not compatible with co-sintering in reducing atmosphere. These sintering conditions will induce detrimental Ni coarsening and Ni–Fe–Cr interdiffusion, consequently degrading performance and material stability [3,4,6,7]. Also, the conventional cathode materials cannot be transferred

* Corresponding author. Tel.: +45 4677 5756; fax: +45 4677 5858.
E-mail address: trkl@risoe.dtu.dk (T. Klemensø).

0378-7753/$ – see front matter © 2011 Elsevier B.V. All rights reserved.
doi:10.1016/j.jpowsour.2011.07.014

directly to metal-supported SOFCs. The cathode materials, such as LSM ($(La,Sr)MnO_3$) and LSCF ($(La,Sr)(Co,Fe)O_3$), typically require sintering at temperatures above 1000 °C to perform well and bond to the electrolyte. However, they are not stable in reducing, inert or vacuum atmosphere, which is required to avoid oxidation of the metal-support during the cathode sintering [3].

A route to meet the electrode processing challenges has been to introduce catalyst impregnation. A metal-supported cell design based on a sintered layered structure with metal-support/porous YSZ layer/dense YSZ electrolyte/porous YSZ layer was developed by LBNL [3,8]. The porous YSZ layers were subsequently impregnated with Ni and LSM, which then act as catalyst and electronic conductor for respectively the anode and the cathode. High initial performance (up to 1 W cm^{-2} at 650 °C) was obtained, but the structure was not stable, with degradation ascribed to sintering of the impregnated Ni anode. The poor stability of Ni impregnation based anodes has also been demonstrated on symmetric anodes [9]. Improved durability has been obtained with metal-supported cermet backbone anodes impregnated with Gd-doped ceria (CGO) and minor amounts of Ni. Galvanostatic testing for 1000 h with a moderate degradation rate of 4.5% kh^{-1}, and initial performance up to 0.4 W cm^{-2} at 650 °C is reported with this design [4]. The co-impregnation of nickel and ceria resulted in enhanced anode stability and performance, which has also been observed on conventional Ni–YSZ anodes [10].

Mixed ionic and electronic conductors, such as LSC ($(La,Sr)CoO_3$) and LSCF, are high performing cathode compositions at intermediate temperatures [2,11–16]. Cathodes of these compositions have been applied to metal-supported SOFCs by either plasma spray, or *in situ* sintering during cell testing to avoid corrosion of the metal-support during the sintering [1,3,4,17]. However, the cobalt-based cathode materials may not be stable in conjunction with the YSZ electrolyte, and react to form low conducting zirconates during fabrication and operation. The reaction is known to take place at high cathode sintering temperatures >1000 °C [2,18], but has also been indicated at intermediate SOFC temperatures ranging down to 650 °C [15,19].

From full ceramic SOFCs it is known that the detrimental interface reaction can be avoided by a CGO diffusion barrier layer between the cathode and the electrolyte. The CGO must be applied by a lower temperature process to avoid interaction between CGO and YSZ, which starts at 1000 °C, and forms poorly conductive solid solution phases [2,20,21]. For ceramic SOFCs, the barrier layers have been applied by screen-printing combined with a sintering step, and physical vapor deposition (PVD) techniques such as magnetron sputtering, electron beam evaporation, and pulsed laser deposition [2,14,18,22]. However, the depositions are carried out at temperatures around 700–800 °C [16,18,19,22], which is too high for metal-supported SOFCs to avoid corrosion of the metal.

In the present study, metal-supported SOFCs fabricated by co-sintering of metal-support, cermet backbone, and electrolyte, are investigated. The cell design include impregnation of the cermet backbone with CGO-Ni to form the active anode, and *in situ* sintered LSCF–CGO (composite) or LSC cathode, in combination with a CGO barrier layer fabricated at a temperature below 450 °C. The investigation focuses on the electrochemical performance and stability of cells containing different barrier layers (spin-coated, magnetron sputtered), and different cermet backbones.

2. Experimental

The half cell (i.e. metal support, anode, electrolyte) processing and infiltration route, described in detail in [4], was also used in this study. This involved tape casting of the layers: metal-support (a Cr-based stainless steel alloy), cermet backbone (with 0–50 vol.% Y-doped ZrO_2 with respect to metal), and electrolyte (ScYSZ, i.e. ZrO_2 co-doped with Sc_2O_3 and Y_2O_3), and then co-sintering of the layers in a reducing atmosphere (H_2/Ar). After co-sintering, the porous metal-support and cermet were infiltrated with the electrocatalytic active phases ($Ce_{0.8}Gd_{0.2}O_{1.9}$ and Ni) to form the active anode (fuel electrode).

Half cells containing three different cermets were fabricated to investigate the effect of different volume fractions of doped zirconia in the cermet on the performance of the cell. The main microstructural effect of varying the ceramic part is changing the specific surface area of the cermet backbone. The three selected cermet backbones are denoted CM1, CM2, CM3, and the amount of doped zirconia in the cermet was varied from 20 to 50 vol.%, with CM1 in the higher range, CM2 in the lower range, and CM3 in the middle range. Samples of the cermet layers were prepared and sintered individually for specific surface area characterization (BET).

Some of the sintered half cells were provided with a PVD barrier layer of CGO10 ($Ce_{0.9}Gd_{0.1}O_{2-\delta}$) on top of the electrolyte layer. The samples were pre-heated to ca. 450 °C to clean the surface before the deposition, which was started and carried out at the same temperature. Reactive pulsed DC magnetron sputtering with an industrial CemeCon CC800/9 Sinox unit was used for the process. Targets with a composition of 88.9 atom% Ce and 11.0 atom% Gd was used (Testbourne Ltd., Hampshire, UK), and the sputtering was done in unipolar pulsed DC mode, in Ar/Kr gas mixture with O_2 as reactive gas, and with a total chamber pressure of ca. 0.4 Pa. The cells were mounted on a two-fold rotation table with a bipolar substrate bias of 50 V (Pinnacle Plus supply, Advanced Energy). The cells were either in electric contact with the table, or insulated from the table with a non-conductive plate, and the obtained films are referred to as "PVDe" and "PVDi", respectively.

Both cells with PVD layer and cells without, were applied with a spin-coated CGO10-based layer, acting as either an additional barrier layer, or as the first barrier layer. The layer will be referred to as "Spin". The wet route spin-coating approach described in [23] was applied using a 2500 rpm rotation speed for 45 s, and the spin-coated layer was subsequently calcined at 350 °C.

The final step in the fabrication is applying the cathode layer by screen-printing. Cathodes with composition 50 vol.% CGO–50 vol.% LSCF ($La_{0.58}Sr_{0.4}Co_{0.2}Fe_{0.8}O_{3-\delta}$–$Ce_{0.9}Gd_{0.1}O_{2-\delta}$) or LSC ($(La_{0.6}Sr_{0.4})_{0.99}CoO_{3-\delta}$) were applied. The layers were fired *in situ* during cell testing at maximum temperature of 800 °C.

Cells with a foot print of 5 cm × 5 cm and an active area of 16 cm^2 (will be referred to as 16 cm^2 cells), and cells with 2 cm × 2 cm foot print and 0.5 cm^2 active area (will be referred to as 0.5 cm^2 cells), were tested electrochemically, with the active area being defined by the screen-printed cathode. The cells were tested in set-ups designed for the two different cell sizes, which are described in more detail in [1,4] and references therein. The main difference between the two set-ups is the gas flow geometry and thus the contacting of the cell. In both cases, platinum meshes are used as contact components, and in the small set-up, alumina tubes are used to lead the gas flow perpendicular onto the 0.5 cm^2 cell and the mesh can be placed flat and parallel with the cell. The big cells on the other hand, are tested in a test house, where the gas flow is laminar and parallel with the cell. In this case, corrugated Pt meshes acting as combined current collector and gas distributor is used.

Polarization curves and impedance data were collected in the temperature range 650–750 °C, with fuel consisting of 4–20 vol.% H_2O on the anode side, and air or O_2 on the cathode side. The air side flow was 128 L h^{-1} (or 8 L h^{-1}cm^{-2} for 16 cm^2 cell) and 6 L h^{-1} (or 12 L h^{-1} cm^{-2} for 0.5 cm^2 cell), and the fuel flow 20 L h^{-1} (or 1.25 L h^{-1}cm^{-2} for 16 cm^2 cell) and 6 L h^{-1} (or 12 L h^{-1}cm^{-2} for 0.5 cm^2 cell). Long-term galvanostatic durability testing was carried out at 650 °C, a current density of 0.25 A cm^{-2}, and low fuel (H_2 + 4% H_2O) and oxygen utilization (<10%). The impedance

Table 1
Summary and nomenclature of the fabricated cells including tested characteristics. BET indicates the specific surface area. The initial ASR is recorded at 650 °C and calculated as the secant value at 0.6 V. Measured degradation rates are shown the relative decrease in cell voltage at 650 °C and 0.25 A cm^{-2} (%kh^{-1}), and the absolute increase in resistance (Ω cm^{-2} kh^{-1}) is shown in brackets. (–) indicates that degradation tests were not performed.

Name	Size (cm^2)	Cermet	Cermet BET (m^2 g^{-1})	Cathode barrier layer	Cathode	ASR (Ω cm^2)	Degradation (%kh^{-1}) or [Ω cm^{-2} kh^{-1}]
CM2-Spin-LSCF #1	0.5	CM2	0.23	Spin	LSCF–CGO	0.52	–
CM2-Spin-LSCF #2	0.5	CM2	0.23	Spin	LSCF–CGO	0.56	–
CM2-Spin-LSC	0.5	CM2	0.23	Spin	LSC	0.50	–
CM1-PVDe-LSC	0.5	CM1	0.31	PVDe + Spin	LSC	0.30	–
CM1-PVDi-LSC	0.5	CM1	0.31	PVDi + Spin	LSC	0.33	–
CM2-PVDe-LSC	0.5	CM2	0.23	PVDe + Spin	LSC	0.27	–
CM2-PVDi-LSC	0.5	CM2	0.23	PVDi + Spin	LSC	0.29	–
CM3-PVDe-LSC #1	0.5	CM3	0.35	PVDe + Spin	LSC	0.34	–
CM3-PVDe-LSC #2	0.5	CM3	0.35	PVDe + Spin	LSC	0.31	1.3 [0.053]
CM1-LSCF-16	16	CM1	0.31	None	LSCF–CGO	0.82	4.5 [0.150]
CM2-Spin-LSCF-16	16	CM2	0.23	Spin	LSCF–CGO	0.64	0.9 [0.036]
CM3-PVDe-LSC-16	16	CM3	0.35	PVDe + Spin	LSC	0.56	1.4 [0.050]

data were recorded with a Solartron 1260 Gain-Phase Analyzer (Solartron Instruments, Houston, TX), using 5 mA amplitude, in the frequency range 0.08 Hz – 82.5 kHz. The data sets were corrected for inductance in the set-up, determined within 2% error, using Kramers–Kronig relation.

The specific surface area (BET) of single cermet layers was measured with an Autosorb 1 (Quantachrome Instruments, Florida), and the surface areas were determined from BET isotherms using krypton adsorption at 78 K. Each measurement was repeated twice, and in some cases also repeated with nitrogen adsorption at 78 K.

Samples for SEM investigations were vacuum embedded in Epofix (Struers, Denmark), ground and polished to 1 μm, and coated with carbon to eliminate surface charging before examination in the microscope. Observations were made with a Hitachi TM1000 tabletop SEM, a Zeiss Crossbeam 1540XB, a Zeiss Supra 25 equipped with an X-ray energy dispersive spectrometer (Carl Zeiss, Konstanz, Germany), and a Nova NanoSEM 600 (FEI Compnay) equipped with an X-ray energy dispersive spectrometer (XEDS), and the XEDS data were recorded with EDAX Genesis software.

An overview of the fabricated and tested samples is seen in Table 1, including a summary of the characteristics and the test results. The nomenclature of the samples introduced in Table 1 will be used in the following.

3. Results and discussion

3.1. Microstructural characterization

A cross-sectional micrograph of a co-sintered half cell is seen in Fig. 1. The metal-support is the thicker porous layer to the right, and the dense electrolyte is seen to the left. In-between is the porous anode cermet layer (CM3 in Fig. 1) into which the electrocatalytic active and mainly ionic conducting CGO-Ni phase is impregnated. The cermet backbone structure is characterized by the specific surface area. Sintered samples of the single cermet layers were characterized with BET, and the variations in the composition and ratio of the cermet layer, resulted in microstructures with specific surface areas of respectively 0.31 m^2 g^{-1} (CM1), 0.23 m^2 g^{-1} (CM2), and 0.35 m^2 g^{-1} (CM3) (cf. Table 1).

SEM micrographs of the three types of barrier layer are seen in Fig. 2. Homogeneous coatings are obtained with the magnetron sputtering in combination with the two-fold rotation table, and furthermore, the layers appear relative dense with PVDi appearing a bit less dense (cf. Fig. 2a) than PVDe (cf. Fig. 2b). In contrast, the spin-coated barrier layer is both uneven in thickness, discontinuous and porous (cf. Fig. 2c).

No major degradation features were observed in the layers or at interfaces during post-test SEM microscopy, except similar corrosion structures as described in detail in [4] were observed in the anode cermet. In [4] the corroded cermet microstructure was ascribed to the increase in pO_2 during operation due the produced steam. The corrosion in these cells could also be caused by leaks, such as gas leakages through sealing or electrolyte and electronic short-circuits. However, the measured equivalent leak currents were small (0.5–40 mA cm^{-2}), flow independent, and relative constant over time, and therefore negligible compared to the amount of water formed during the galvanostatic test with current load of 0.25 A cm^{-2}. A more quantitative analysis of the corrosion features and the mechanisms will require e.g. detailed TEM and STEM (scanning transmission electron microscopy), which is outside the scope of this paper.

No reactions between cathode and electrolyte were detected at the interfaces during post-test SEM-EDS analyses. However, this may solely be due to the resolution limit in the SEM-EDS. From literature it is well-known that the potential zirconate reaction product ($SrZrO_3$) is difficult to distinguish. Even for ceramic SOFCs with cobalt-based cathodes, which experienced much higher processing temperatures and thus more extensive zirconate formation, the

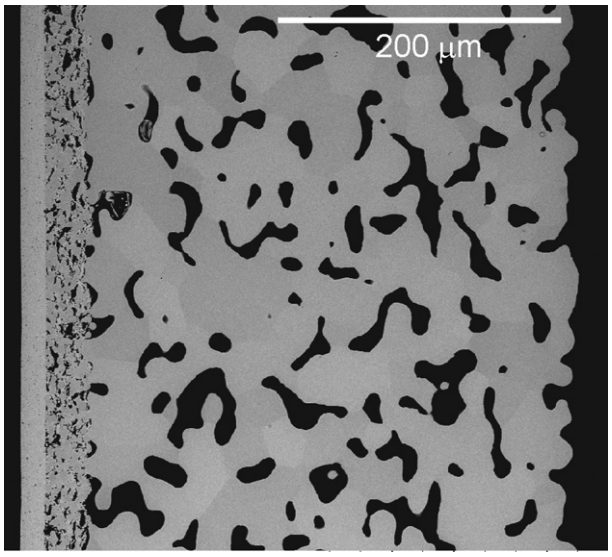

Fig. 1. SEM image of a polished cross-section of a co-sintered half cell. The dense layer to the left is the electrolyte, followed by the cermet layer (CM3), and the metal-support.

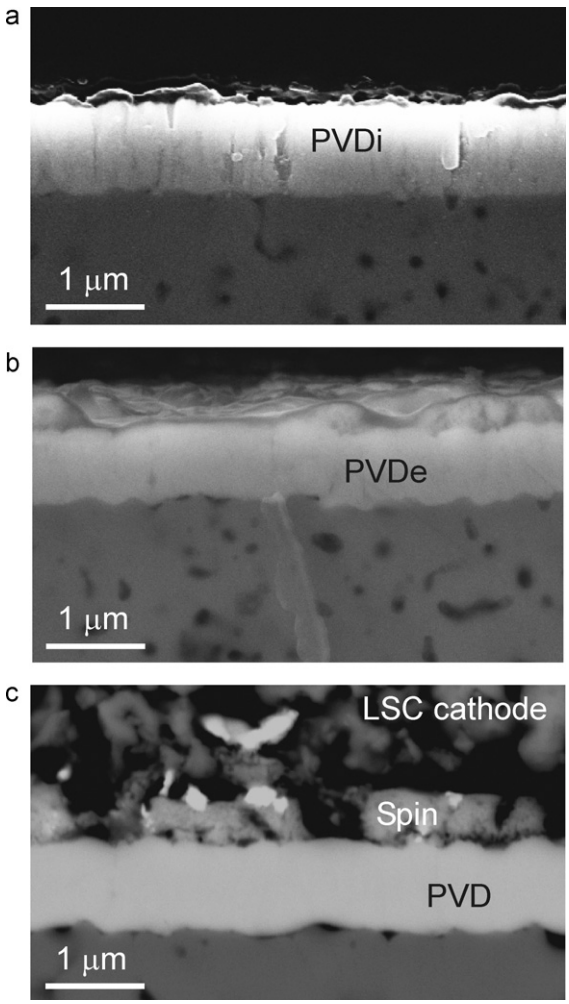

Fig. 2. SEM images of the different CGO barrier layers (a) PVDi, (b) PVDe and (c) Spin.

zirconate phase appeared as nano-sized islands only discernable with TEM [2,18]. For lower temperature processing and -test, zirconates have only been detected indirectly using GAXRD (glancing angle X-ray diffraction) and TEM e-beam diffraction [19], or SIMS (secondary ion mass spectrometry) which indicated a $SrZrO_3$ rich phase in the depth profile with a thickness of ca. 150 nm, formed at the LSC–YSZ interface after 3800 h at 700 °C [15]. For the samples in this study, either advanced TEM or SEM is believed required to distinguish any formed zirconates. With advanced SEM microscopy with a field emission gun equipped with WDS detectors, a chemical resolution below 100 nm is possible. Such advanced studies are outside the scope of this paper but are in progress for further verification of the interface composition, and will be reported in a future publication.

Micrographs of the two types of cathodes are seen in Fig. 3. The LSC cathode appears very homogeneous (cf. Fig. 3a), whereas the composite LSCF–CGO is less well packed and contains coarser porosities and agglomerates (cf. Fig. 3b).

3.2. Electrochemical characterization of 0.5 cm^2 active cells

Polarization curves recorded at 650 °C for button cells with either LSCF–CGO or LSC cathodes are shown in Fig. 4. The cells contain in all cases CM2 cermet and a (porous) spin-coated barrier layer. The difference between the two identical cells, CM2-Spin-LSCF #1 and #2, is the maximum start-up temperature during cell

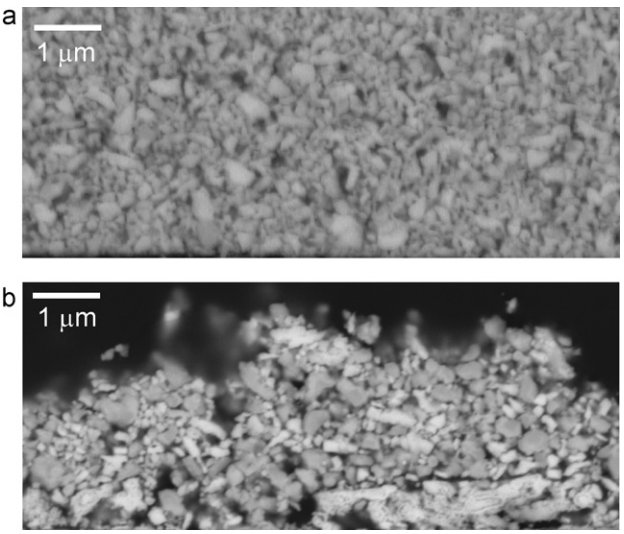

Fig. 3. Post-test micrographs of (a) LSC cathode and (b) the composite LSCF–CGO cathode.

test, which was 50 °C lower for CM2-Spin-LSCF #1 than for all other tested cells in this study. Very similar performance of the cells is seen, with the initial area specific resistance (ASR, calculated as the secant value at 0.6 V) varying between 0.50 and 0.56 Ω cm^2 (cf. Fig. 4 and Table 1). The best performance was obtained with the LSC cathode (0.50 Ω cm^2). Furthermore, a slightly lower ASR was obtained for CM2-Spin-LSCF #1 that experienced 50 °C lower start-up temperature than for CM2-Spin-LSCF #2 (0.52 Ω cm^2 versus 0.56 Ω cm^2).

The LSC cathode is known to perform better at intermediate temperatures than pure LSCF due to the higher electrical conductivity and higher catalytic activity. In [13] the maximum power density was 31% higher for cells containing LSC cathode compared to corresponding cells with LSCF cathode. However, for the current metal-supported cells, the difference between the LSC and LSCF–CGO performance is less than 12%. The comparable performances could be related to the composite LSCF–CGO cathode. The electrocatalytic activity of LSCF can be significantly improved by adding a highly oxygen ion conducting phases such as Gd-doped CeO_2 [24,25], and a factor of 10 decrease in polarization resis-

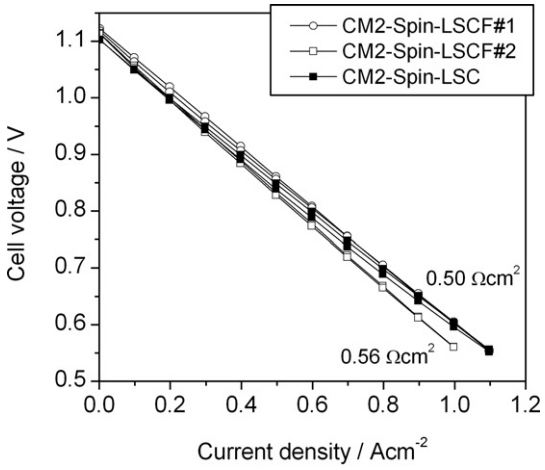

Fig. 4. Electrochemical performance of metal-supported cells with 0.5 cm^2 active cell area. The cells contained CM2 type anode, and spin-coated barrier layer, and either LSCF–CGO or LSC cathode. The data were recorded at 650 °C with 96% H_2–4% H_2O as fuel, and air as oxidant. The inserted numbers are calculated highest and lowest area specific resistance.

tance has been reported when 50 vol.% CGO was added to LSCF [26]. However, the cathode performance is also strongly dependent on the microstructure [27], and the presence of agglomerates such as those seen in the composite cathode in Fig. 3b, will decrease the performance significantly, and could add to the explanation of the similarity to the LSC cathode.

Another, or additional, explanation to the observed similar performance of the two different cathode materials, is zirconate formation. Based on the micrographs, the porous spin-coated barrier layer does not appear capable of preventing Sr-diffusion (cf. Fig. 2c), and the zirconate formation would be worse in the case with the more reactive LSC. This would result in a lower performance with the LSC cathode, despite the homogeneous appearance. Furthermore, a role played by zirconates is indicated by the slightly better performance of the cell which experienced a 50 °C lower start-up temperature (CM2-Spin-LSCF #1), and thus slightly less favorable conditions for zirconate growth.

Fig. 5 shows polarization characteristics for button cells with dense PVD barrier layers in combination with LSC cathode. Compared to the samples in Fig. 4, the ASR values are decreased with 32–46% (cf. Table 1). This strongly indicates Sr-diffusion and zirconate formation if the barrier layer is not dense, as in the case with the spin-coated layers (cf. Fig. 4), and prevention of Sr-diffusion with the dense PVD layer (cf. Fig. 5). Furthermore, for both CM1 and CM2 based cells, slightly lower ASR is seen with PVDe than PVDi, and this corresponds well with the apparent higher density for PVDe (Fig. 2b) compared to PVDi (Fig. 2a). The lowest ASR (0.27 Ω cm^2) corresponds to a maximum power density of 1.14 W cm^{-2}, which is a performance remarkably better than for the conventional Ni–YSZ supported ceramic cells with LSM–YSZ composite cathode, showing ASR in the range of 0.5 Ω cm^2 at 750 °C [28], and also better than ceramic cells with LSC cathode in combination with barrier layer, which have reported ASR of 0.37–0.64 at 650 °C [29].

EIS measurements were conducted to further characterize the cells. Data are represented with Nyquist plot and Bode plot of the imaginary part of the complex impedance data. The Bode plot is further combined with selected ADIS (analysis of differences in impedance spectra) spectra. ADIS is a way of visualizing differences between two spectra by looking at the differences between the real part derivatives of the two Bode spectra [30]. Fig. 6a shows the plots for CM2 cells with different barrier layers, and the corresponding

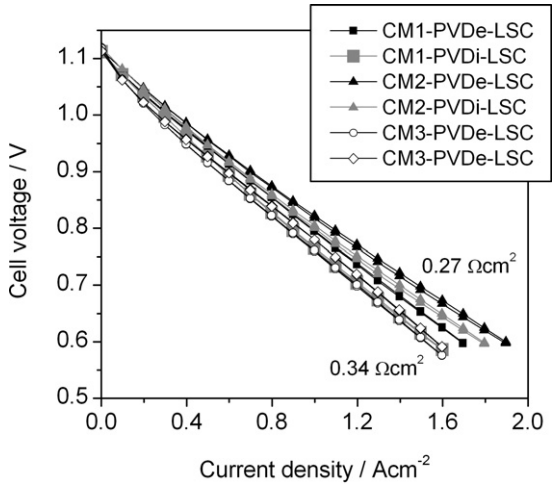

Fig. 5. Electrochemical performance of metal-supported cells with 0.5 cm^2 active cell area. The cells contained different types of anode cermet (CM1,2,3) and different types of PVD barrier layers in combination with spin-coated CGO and LSC cathode. The data were recorded at 650 °C with 96% H_2–4% H_2O as fuel, and air as oxidant. The inserted numbers are calculated highest and lowest area specific resistance.

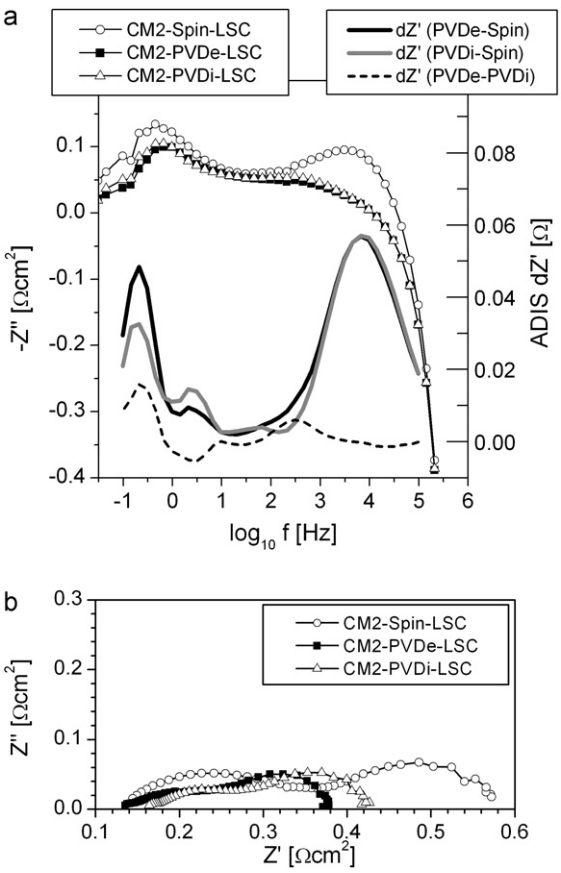

Fig. 6. (a) Combined Bode and ADIS representations of CM2 based cells with different barrier layers in combination with LSC cathode. (b) The corresponding Nyquist plot.

Nyquist plot is seen in Fig. 6b. Based on Fig. 6 it appears that the higher impedance of the cell with only spin-coated barrier layer (CM2-Spin-LSC in Fig. 4) versus the cells with PVD barrier layers (CM2-PVDe-LSC and CM2-PVDi-LSC in Fig. 5) originates from a high frequency process in the 10 kHz range. This fits well with the presence of a zirconate at the cathode interface, restricting the oxide ion charge transfer processes from the cathode to the electrolyte. Cathode charge transfer processes are known to occur within this frequency range. A summit frequency around 1 kHz at 750 °C for LSCF–CGO cathode [26] has been reported, and for LSM–YSZ cathodes at 850 °C, a summit frequency of 40 kHz was reported [27].

Comparing the cells with PVDe barrier layer in Fig. 5, a slightly better performance is seen for the CM2 based cell than for CM1, which again is slightly better than the CM3 based cells. The order of increase in performance is seen to correlate with the decrease in specific surface area of the cermet (cf. Section 3.1 and Table 1). The combined Bode and ADIS representation of these cells and the corresponding Nyquist plot is shown in Fig. 7a and b. The main difference between these spectra appear in the low frequency range around 1 Hz. Thus, the difference between the corresponding PVDe cells with different cermets does not appear to be electrochemical but due to minor differences in the gas diffusion in porous structures, which is a known process occurring in this frequency range [4].

The cells were also characterized using EIS measurements at different temperatures (650–750 °C), with either air or oxygen as oxidant, and with different fuel flows (50, 100, 500 ml min^{-1}). As an example, Nyquist and Bode representations of the impedance responses of the cell type CM2-PVDe-LSC are displayed in Fig. 8a and b. Decreasing the temperature (while keeping fuel constant at

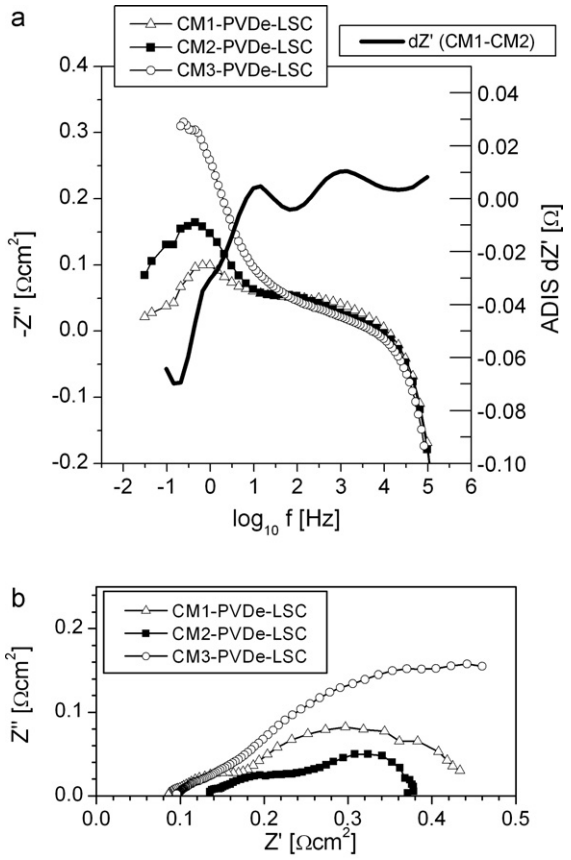

Fig. 7. (a) Combined Bode and ADIS representations of cells with different half cell types (CM1,2,3) in combination with PVDe, spin-coated CGO, and LSC cathode. (b) Corresponding Nyquist plot.

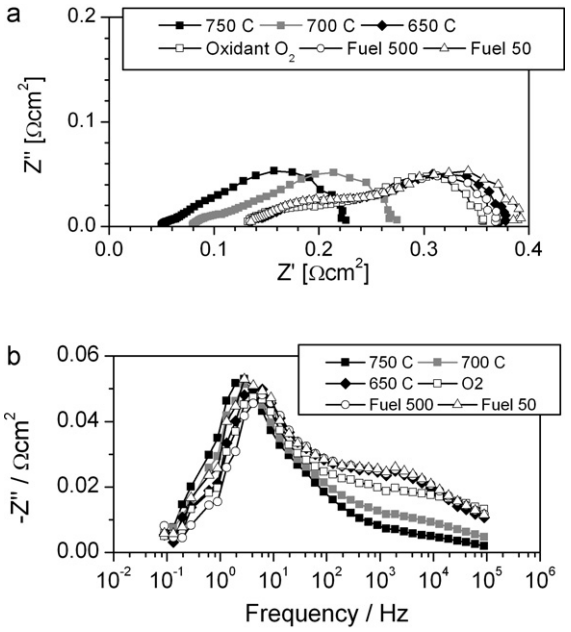

Fig. 8. Electrochemical impedance data for a CM2 based cell with PVDe and LSC cathode (CM2-PVDe-LSC). Data are recorded at temperatures 650, 700, 750 °C, with air as oxidant and humidified hydrogen (96% H_2–4% H_2O) as fuel with standard flows of 100 ml min^{-1}. At 650 °C, the oxidant was changed to O_2, and the fuel flow was varied from 0.5 to 5 times the standard flow of 100 ml min^{-1}. The data are represented as (a) Nyquist and (b) Bode plot.

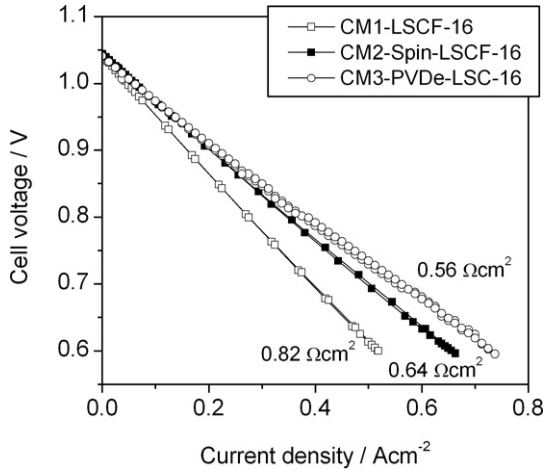

Fig. 9. Electrochemical performance of metal-supported cells with 16 cm^2 active cell area, different cermet backbone (CM1,2,3), barrier layers (none, spin-coated, and PVDe), and cathodes (LSCF–CGO, LSC). The curves are recorded at 650 °C with 80% H_2–20% H_2O as fuel, and air as oxidant. The inserted numbers are the calculated area specific resistance.

100 ml min^{-1} H_2–4% H_2O and 100 ml min^{-1} air as oxidant) results in increasing impedance, with the increase occurring in the higher frequency range (>100 Hz). Changing oxidant from air to O_2 at a constant temperature of 650 °C is also seen to create a response in the range of above 100 Hz. Initial symmetrical cell testing shows perfect overlap of the anode and cathode electrochemical processes, complicating deconvolution in this case, as opposed to conventional ceramic cells with Ni–YSZ anode and LSM–YSZ cathode, where the electrode processes are distributed over several decades of frequencies [27]. Thus, to separate the processes further, more advanced impedance analyses are required. DRT (distribution of relaxation times) data treatment combined with CNLS (complex nonlinear least square) fitting may be used to achieve a complete deconvolution of these types of cells, but is outside the scope of this paper.

The low frequency end of the impedance spectra in Fig. 8 appears to be temperature independent, which indicate gas concentration related impedances (diffusion and possibly conversion). Since the spectra appears to be only slightly sensitive to variations in the fuel flow at constant temperature of 650 °C, with lower flow (50 ml min^{-1}) resulting in a slight increase, and higher flow (500 ml min^{-1}) in a slight decrease, diffusion in the porous structures is indicated to be the main contributor to this part. For further details on diffusion and conversion impedances see [31,32].

3.3. Electrochemical characterization of 16 cm^2 active cells

Some of the button cell tests have been reproduced on a 16 cm^2 cell level (cf. Table 1). Fig. 9 shows the polarization curves for the cell design CM2 with only spin-coated barrier layer in combination with LSCF–CGO cathode, and CM3 with PVDe in combination with LSC cathode. For comparison, the previously reported data on a 16 cm^2 cell with CM1 without any barrier layer and LSCF–CGO cathode [4] is included in the graph. The data are recorded at 650 °C with 80% H_2–20% H_2O as fuel, and air as oxidant.

For these cells, the best performance (ASR 0.56 Ω cm^2) is observed for the CM3 with the dense PVDe barrier layer, and the high performing homogeneous LSC cathode. Though, it is not in the same range as for the corresponding button cells (ASR 0.34 Ω cm^2, cf. Fig. 5 and Table 1), it is the best performance demonstrated and reported on the 16 cm^2 metal-supported cell. For the other tested 16 cm^2 cells (CM1-LSCF-16 and CM2-Spin-LSCF-16), a sim-

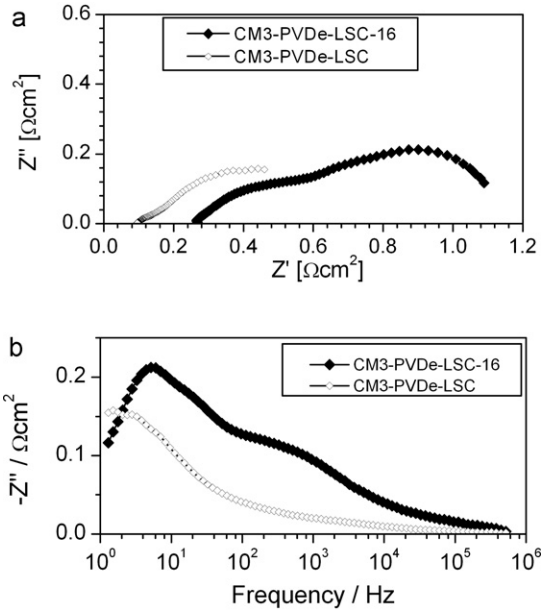

Fig. 10. Electrochemical impedance data for corresponding CM3 cells with active areas of 0.5 and 16 cm^2, respectively. Data are recorded at temperatures 650 °C, and with air as oxidant, and humidified hydrogen (96% H_2–4% H_2O) as fuel. The data are represented as (a) Nyquist and (b) Bode plot.

ilar discrepancy to the corresponding button cell performance is observed.

The disagreements between the different cell levels are believed to be related to contacting issues in the 16 cm^2 cell test set-up. As described in Section 2, the contacting of the 16 cm^2 cells is based on corrugated platinum meshes acting as combined current collector and gas distributor. To facilitate the latter, the mesh must not experience much pressure as it will collapse, but still needs some pressure to have stable contact to the cell and outer test house. For the 0.5 cm^2 button cells on the other hand, the contacting area is smaller and the current collecting platinum mesh is planar and not pressure dependent, since the gas flow in this set-up is perpendicular to the cell, as opposed to parallel in the 16 cm^2 set-up. Fig. 10 shows Nyquist and Bode plot for corresponding CM3 based cells, where the only difference is the active area of 0.5 and 16 cm^2, respectively. It is seen that the Nyquist plot of the 16 cm^2 cell is shifted to the right, and in addition shows higher polarization resistance. This strongly indicates current constriction/current distribution issues with the 16 cm^2 corrugated mesh set-up. Limited current distribution is known to be associated with higher serial resistance, as well as higher polarization resistance due to the lower effective electrode area. The inadequate current distribution phenomenon is analogous to the well-described situation present when measurements are conducted on thin films with significant sheet resistance, cf. [33].

The 16 cm^2 contacting route with corrugated meshes is well-established for full ceramic cells, e.g. used in [27,28], and the observed current distribution issues associated with the set-up in this case is therefore believed to be related to the *in situ* sintered cathodes. Cathodes that are not fully sintered (as the cathodes in this study which experienced maximum 800 °C for a short amount of time) may change conductivity as well as dimension with time, even at constant temperature. Thus, the critical pressure on the mesh to establish sufficient contact may vary with time, but in the set-up the pressure is fixed from the beginning. To verify and avoid the issue with contacting further, alternative contacting routes are being investigated for future cells to be tested with *in situ* sintered cathodes.

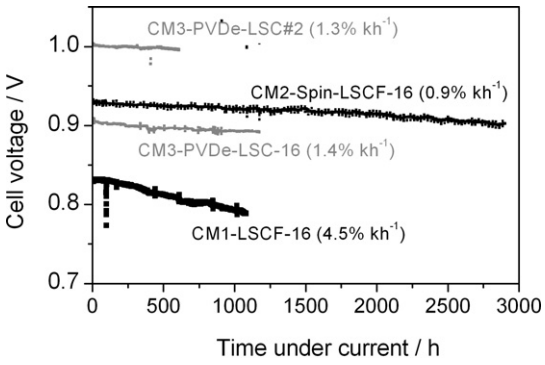

Fig. 11. Galvanostatic durability curves of the metal-supported cells with active areas of 0.5 or 16 cm^2, tested at 650 °C with a current density of 0.25 A cm^{-2}, and 96% H_2–4% H_2O as fuel, and air as oxidant. Both the CM3 based cells have PVDe and spin-coated barrier layers in combination with LSC cathode. The CM1 and CM2 based cells have LSCF–CGO cathodes, and CM2 has a spin-coated barrier layer.

Despite the limitations of the set-up, some of the best reported 16 cm^2 cell test could be obtained, as well as durability data. Fig. 11 shows the evolution in cell voltage over time for the 16 cm^2 cells with different designs (cf. Table 1). For comparison, the previously reported durability of the CM1 based cell in [4] has been included, as well as the curve for a button cell with low ASR. The stability tests were in all cases carried out at a current density of 0.25 A cm^{-2}, at 650 °C, and with 96% H_2–4% H_2O as fuel, and air as oxidant (fuel and oxygen utilization below 10%).

A significant improvement in stability is seen for the CM2 and CM3 based cell design, irrespective of the quality of barrier layer, the cathode or the cell size. In the best case (CM2-Spin-LSCF-16), the degradation is improved to 0.9% kh^{-1} compared to the 4.5% kh^{-1} observed for the first CM1 based cell. Furthermore, the degradation rate of 0.9% kh^{-1} is demonstrated to be steady for up to 3000 h test under the selected test conditions.

The slightly better stability observed for the cell with only spin-coated barrier layer (CM2-Spin-LSCF-16, 0.9% kh^{-1}) compared to the cells with PVDe barrier layers (CM3-PVDe-LSC-16 and CM3-PVDe-LSC, 1.3–1.4% kh^{-1}), indicates that the main degradation mechanism is not continous zirconate growth. Also, the similar degradation rates of the corresponding CM3 cells of size 0.5 and 16 cm^2 suggest that degradation in the contacting degree over time of the 16 cm^2 is not an issue. The most likely degradation mechanisms are believed to be anode cermet corrosion, as previously suggested in [4], or related to changes in the *in situ* sintered cathodes. The cells were characterized by EIS after the durability testing, but due to the overlapping electrode processes, in combination with the low degradation, further characterization of the degradation mechanisms were not possible in this study. Detailed electrochemical analyses including symmetrical cell test are in progress and will be reported in a future publication. It is however indicated that anode corrosion partly explains the degradation, since slightly higher degradation rates are seen for CM3 (and CM1), which have higher anode surface area compared to CM2 (cf. Section 3.1 and Table 1), and thereby also have a higher surface areas exposed during cell operation.

4. Conclusions

The metal-supported SOFC design developed at Risø DTU is demonstrated to have electrochemical performance potential beyond the state-of-the-art anode-supported SOFC. This is achieved by introducing a dense CGO barrier layer in combination with Sr-doped lanthanum cobalt oxide (LSC) cathode. Area specific resistances (ASR) down to 0.27 Ω cm^2, corresponding to a maximum power density up to 1.14 W cm^{-2} at 650 °C can be obtained

with barrier layers fabricated by magnetron sputtering. The initial performance depends on the density of the barrier layer, indicating that Sr^{2+} diffusion and $SrZrO_3$ formation is an issue even at the investigated intermediate SOFC temperature.

Significant improvement in stability of the metal-supported design is also demonstrated possible. Steady degradation rates of $0.9\%\,kh^{-1}$ in cell voltage, corresponding to a resistance increase of $0.036\,\Omega\,cm^{-2}\,kh^{-1}$, for up to 3000 h galvanostatic testing at 650 °C was observed. Anode corrosion in combination with changes in the *in situ* sintered cathode are possible degradation mechanisms.

Acknowledgements

The work was financially supported by Topsoe Fuel Cell A/S, the Danish National Advanced Technology Foundation, the EU project FP7-211940 (METSOFC), and NordForsk ref. no. 9346. The authors thank the Fuel Cells and Solid State Chemistry Division at Risø DTU for assistance.

References

[1] P. Blennow, J. Hjelm, T. Klemensø, Å. Persson, K. Brodersen, A.K. Srivastava, H.L. Frandsen, M. Lundberg, S. Ramousse, M. Mogensen, ECS Trans. 25 (2) (2009) 701–710.
[2] R. Knibbe, J. Hjelm, M. Menon, N. Pryds, M. Søgaard, H.J. Wang, K. Neufeld, J. Am. Ceram. Soc. 93 (9) (2010) 2877–2883.
[3] M.C. Tucker, J. Power Sources 195 (15) (2010) 4570–4582.
[4] P. Blennow, J. Hjelm, T. Klemensø, S. Ramousse, A. Kromp, A. Leonide, A. Weber, J. Power Sources (2010) 088, doi:10.1016/j.powsour.2010.08.
[5] C.-S Hwang, C.-H. Tsai, J.-F. Yu, C.-L. Chang, J.-M. Lin, Y.-H. Shiu, S.-W. Cheng, J. Power Sources 196 (2011) 1932–1939.
[6] R. Vassen, D. Hathiramani, J. Mertens, V.A.C. Haanappel, I.C. Vinke, Surf. Coat Technol. 202 (2007) 499–508.
[7] M. Brandner, M. Bram, J. Froitzheim, H.P. Buchkremer, D. Stöver, Solid State Ionics 179 (2008) 1501–1504.
[8] M.C. Tucker, G.Y. Lau, C.P. Jacobsen, L.C. DeJonghe, S.J. Visco, J. Power Sources 175 (2008) 447–451.
[9] T. Klemensø, K. Thydén, M. Chen, H.-J. Wang, J. Power Sources 195 (2010) 7295–7301.
[10] J. Qiao, K. Sun, N. Zhang, B. Sun, J. Kong, D. Zhou, J. Power Sources 169 (2007) 253–258.
[11] R. Küngas, F. Bidrawn, J.M. Vohs, R.J. Gorte, Electrochem. Solid-State Lett. 13 (2010) B87–B90.
[12] Y. Tao, J. Shao, W.G. Wang, J. Wang, Fuel Cells 5 (2009) 679–683.
[13] C. Torres-Garibay, D. Kovar, A. Manthiram, J. Power Sources 187 (2009) 480–486.
[14] N. Jordan, W. Assenmacher, S. Uhlenbruck, V.A.C. Haanappel, H.P. Buchkremer, D. Stöver, W. Mader, Solid State Ionics 179 (2008) 919–923.
[15] M. Sase, D. Ueno, K. Yashiro, A. Kaimai, T. Kawada, J. Mizusaki, J. Phys. Chem. Solids 66 (2005) 343–348.
[16] F. Zhao, L. Zhang, Z. Jiang, C. Xia, F. Chen, J. Alloys Compd. 487 (2009) 781–785.
[17] Y.-M. Kim, P. Kim-Lohsoontorn, J. Bae, J. Power Sources 195 (2010) 6420–6427.
[18] S. Uhlenbruck, T. Moskalewicz, N. Jordan, H.-J. Penkalla, H.P. Buchkremer, Solid State Ionics 180 (2009) 418–423.
[19] H.-S. Noh, J.-W. Son, H. Lee, J.-S. Park, H.-W. Lee, J.-H. Lee, Fuel Cells 10 (2010) 1057–1065.
[20] X.-D. Zhou, B. Scarfino, H.U. Anderson, Solid State Ionics 175 (2004) 19–22.
[21] A. Tsoga, A. Gupta, A. Naoumidis, D. Skarmoutsos, P. Nikolopoulos, Ionics 4 (1998) 234–240.
[22] S. Uhlenbruck, N. Jordan, D. Sebold, H.P. Buchkremer, V.A.C. Haanappel, D. Stöver, Thin Solid Films 515 (2007) 4053–4060.
[23] P. Plonczak, M. Joost, J. Hjelm, M. Søgaard, M. Lundberg, P.V. Hendriksen, J. Power Sources 196 (2011) 1156–1162.
[24] A. Esquirol, J. Kilner, N. Brandon, Solid State Ionics 175 (2004) 63–67.
[25] Y. Leng, S.H. Chan, Q. Liu, Int. J. Hydrogen Energy 33 (2008) 3808–3817.
[26] E.P. Murray, M.J. Sever, S.A. Barnett, Solid State Ionics 148 (2002) 27–34.
[27] R. Barfod, M. Mogensen, T. Klemensø, A. Hagen, Y.-L. Liu, P.V. Hendriksen, J. Electrochem. Soc. 154 (4) (2007) B371–B378.
[28] A. Hagen, M. Menon, R. Barfod, P.V. Hendriksen, S. Ramousse, P.H. Larsen, Fuel Cells 06 (2) (2006) 146–150.
[29] J. Hjelm, M. Søgaard, R. Knibbe, A. Hagen, M. Mogensen, ECS Trans. 13 (26) (2008) 285–299.
[30] S.H. Jensen, A. Hauch, P.V. Hendriksen, M. Mogensen, N. Bonanos, T. Jacobsen, J. Electrochem. Soc. 154 (2007) B1325–B1330.
[31] T. Jacobsen, P.V. Hendriksen, S. Koch, Electrochim. Acta 53 (2008) 7500–7508.
[32] W.G. Bessler, Proceedings of 7th Eur. SOFC Forum, 2006.
[33] J. Nielsen, T. Jacobsen, Electrochim. Acta 55 (2010) 6248–6254.